JACS
JOURNAL OF THE AMERICAN CHEMICAL SOCIETY

Article

pubs.acs.org/JACS

Enhanced Mass Transport of Electroactive Species to Annular Nanoband Electrodes Embedded in Nanocapillary Array Membranes

Sean P. Branagan,[‡] Nicholas M. Contento,[‡] and Paul W. Bohn*[,‡,†]

[‡]Department of Chemical and Biomolecular Engineering and [†]Department of Chemistry and Biochemistry, University of Notre Dame, Notre Dame, Indiana 46556, United States

Supporting Information

ABSTRACT: Electroosmotic flow (EOF) is used to enhance the delivery of $Fe(CN)_6^{4-}/Fe(CN)_6^{3-}$ to an annular nanoband electrode embedded in a nanocapillary array membrane, as a route to high efficiency electrochemical conversions. Multilayer Au/polymer/Au/polymer membranes are perforated with 10^2–10^3 cylindrical nanochannels by focused ion beam (FIB) milling and subsequently sandwiched between two axially separated microchannels, producing a structure in which transport and electron transfer reactions are tightly coupled. The middle Au layer, which contacts the fluid only at the center of each nanochannel, serves as a working electrode to form an array of embedded annular nanoband electrodes (EANEs), at which sufficient overpotential drives highly efficient electrochemical processes. Simultaneously, the electric field established between the EANE and the QRE (>10^3 V cm^{-1}) drives electro-osmotic flow (EOF) in the nanochannels, improving reagent delivery rate. EOF is found to enhance the steady-state current by >10× over a comparable structure without convective transport. Similarly, the conversion efficiency is improved by approximately 10-fold compared to a comparable microfluidic structure. Experimental data agree with finite element simulations, further illustrating the unique electrochemical and transport behavior of these nanoscale embedded electrode arrays. Optimizing the present structure may be useful for combinatorial processing of on-chip sample delivery with electrochemical conversion; a proof of concept experiment, involving the generation of dissolved hydrogen *in situ* via electrolysis, is described.

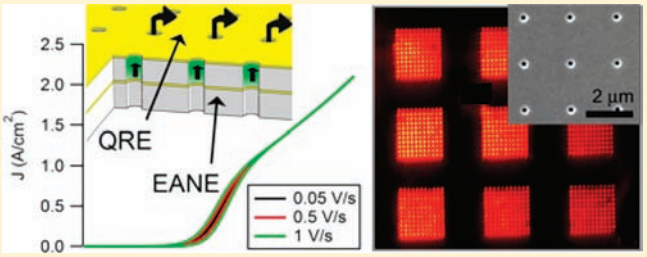

INTRODUCTION

Nanoelectrodes categorically exploit the transition from planar to hemispherical diffusion that occurs as the size of the electrode approaches the diffusive scaling length.[1,2] Improved sensitivity, faster detection, and signal amplification by redox cycling are a few of the benefits that accrue, all of which have been demonstrated within planar thin film electrodes.[3−5] Similarly, a network of planar microelectrodes can be used to support electrokinetic (EK) flow within micrototal analysis systems (μTAS), for example, by leveraging electroosmotic flow (EOF).[6,7] Despite this overlap, EOF is rarely used in combination with analytical electrochemistry due to important technical challenges: (1) ion migration, which causes a background current convoluted with the desired redox current; and (2) solvent electrolysis, which tends to occur whenever the applied potential is sufficiently great to drive EOF.[8,9] Both have been explored in detail using bipolar electrodes in microchannels by Crooks et al.[10,11] Convective delivery of electrochemical reagents within microfluidic systems is typically accomplished with an external pump, which is hardly compatible with μTAS.[12−14]

Despite the technical challenges, there are good reasons to explore ways in which EOF may be advantageously combined with nanoelectrochemistry. For example, the need for compact, multifunctional elements is widely recognized in μTAS,[15] and advances in fabrication have produced increasingly sophisticated three-dimensional micro/nanofluidic chips over the past decade. For example, nanofluidic interconnects between microfluidic channels have been shown to support electrokinetic (EK) flow combined with mass-limited sample control,[16] size- and charge-selective separation,[17] preconcentration,[18,19] sensing,[20,21] and chemical reactivity within nanopores.[22] However, little has been done to incorporate nanoscale electrodes within nanofluidic volumes supporting EK flow, although the benefits of both for electrochemistry are well documented.[23,24] For example, the transition point between steady-state and transient operation of a glass nanopore electrode can be manipulated by varying the nanopore depth.[25,26] However, electrochemical signals from glass nanopores are hampered by the lack of convective transport and by electrostatic gating at the mouth of the device.[27,28] Although the latter difficulty can be overcome by parallelization,[29] the structures are not ideal for reactive processing, because a diffusive boundary layer rapidly forms, restricting reactant delivery to the electrode surface.[30]

The goal of the present work is to demonstrate the use of EOF to enhance electrochemical reactivity at a nanoelectrode,

Received: February 21, 2012
Published: April 16, 2012

dx.doi.org/10.1021/ja3017158 | J. Am. Chem. Soc. 2012, 134, 8617−8624

within nanochannels, in a way that is broadly compatible with μTAS architectures.[15] The experiments presented here, together with supporting theory and finite element simulations, demonstrate that nanocapillary array membranes (NCAMs) supporting embedded annular nanoband electrodes (EANEs) are well-suited to coupling nanoelectrochemistry with convective reagent delivery, because: (1) the applied potential necessary to achieve fields large enough to drive EOF is reduced, (2) electrochemical reactions can be performed at very high efficiency due to rapid radial diffusion within the nanopore, and (3) throughput similar to a microchannel can be achieved via parallel construction of up to ~1000 nanochannels (~2.5 × 10^7 pores cm^{-2}) to form an EANE array.[31] The present nanoelectrode−nanochannel system outperforms a microband electrode−microchannel system operated under similar conditions.[32] Finally, to demonstrate the utility of the NCAM-EANE construct, hydrogen is produced electrolytically at levels appropriate for use in a downstream hydrogenation reaction.[33]

To realize a NCAM-EANE array, a freestanding membrane is perforated by 10^2−10^3 vertically aligned nanochannels to produce an NCAM, and is used to establish fluidic contact between two axially separated microchannels, Figure 1A. The large number of closely spaced parallel nanochannels is designed to enhance throughput. The membrane is constructed from a 4-layer Au/polymer/Au/polymer structure, Figure 1C. The middle Au layer intersects all of the nanochannels at the center of the membrane, forming an EANE that isolates electrochemical reactions from solution, except at the center of the nanopores, Figure 1D. The top Au layer functions as a built-in quasi-reference/counter electrode (QRE). Sample is delivered to the EANE by EOF driven by the electric field between the EANE and the QRE. Solvent electrolysis, a commonly encountered problem of electrified fluids in microstructures, is mitigated by locating the electrodes sufficiently close to realize a large field strength (>10^3 V/cm) at a relatively low applied potential (<1 V).

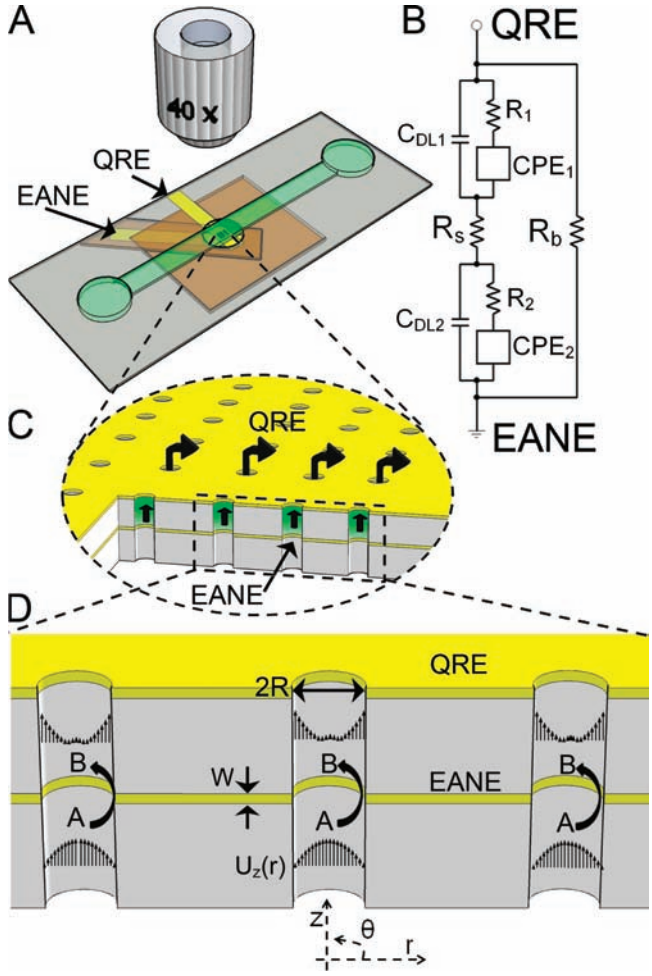

Figure 1. (A) Schematic diagram showing the macroscopic layout of the device. Bottom microchannel not shown for clarity; (B) circuit diagram corresponding to electron transfer at the QRE and EANE; (C) schematic cross section showing relative locations of the QRE, EANE, and nanochannels; (D) magnified view of the EANE depicting locations of an arbitrary reaction A → B at the EANE, with flow profiles and geometric parameters. Drawings not to scale.

EXPERIMENTAL SECTION

A detailed description of the NCAM-EANE fabrication process is given in the Supporting Information (SI). A brightfield micrograph of a typical sample is shown in Figure 2A, with increasing magnification shown by the SEMs in Figure 2B,C. The pores are milled in 11 × 11 blocks of 121 pores, Figure 2B, with up to 9 blocks per sample, Figure 2A. The thicknesses of the top and bottom SU-8 layers, as measured by SEM, are 7.0 ± 0.5 and 6.8 ± 0.6 μm respectively, cf. Figure 2D, and the axial width of the EANE is 195 ±7 nm, Figure 2E. Including the QRE, the total membrane thickness (pore length) is ~15 μm. Membranes with pore diameters ranging from 120 nm < d < 1 μm were fabricated; the pore diameter of the EANE array shown in Figure 2A−C is ~500 nm, while that of the EANE cross-sectioned in Figure 2 D,E is ~120 nm with slight broadening near the mouth of the pore to ~150 nm. The very high aspect ratio, depth/diameter ≈100, much greater than similar nanopores demonstrated in Au/SiN_x bilayer membranes, contributes to the ability of the NCAM-EANE array to support EOF.[21,34] Comprehensive electrochemical characterization was performed on two representative devices. The first was used for electrochemical characterization in ferri/ferrocyanide solutions and contained a single block of 121 pores with a pore diameter of ca. 600 nm, for a total EANE area of ~4.7 × 10^{-7} cm^2. The second device was used in the demonstration of hydrogen generation *in situ* and contained nine blocks of 121 pores for a total of 1089 pores, with a pore diameter of 500 nm resulting in a nominal electrode area of 3.4 × 10^{-6} cm^2. Previous studies from this laboratory used similar structures constructed from poly(methylmethacrylate-*co*glycidylmethacrylate), but these structures showed significant cracking of both the polymer and Au layers,[35] rendering them unusable for electrochemistry. The Au/SU-8 structures used here exhibit no cracking under normal use, consistent with behavior of other microfluidic structures prepared in SU-8.[36]

A QRE is used instead of a standard reference electrode, for example, Ag/AgCl, for all experiments, because: (1) a nearby reference electrode greatly reduces ohmic losses; (2) the fabrication process requires a top Au surface to prevent electrostatic charging of the FIB substrate; (3) locating the electrode close to the EANE results in an electric field sufficiently large to drive EOF; and (4) device complexity is reduced, a desirable characteristic for μTAS applications.[37] The proximity of the QRE to the EANE would normally present the possibility of undesirable redox cycling, which may occur whenever EK transport sweeps the electrochemical product toward the QRE. Under these flow conditions, this undesired phenomenon is likely to consume products generated at the EANE, leaving a low net conversion of reactants. This possibility, which is discussed in more detail later, is eliminated in practice simply by directing EK flow away from the QRE. Alternatively, when EOF is directed toward the QRE and redox cycling is a possibility, a useful microenvironment is still maintained between the EANE and the QRE, containing a high concentration of the electrochemical product for possible consumption in a downstream process reaction.[33]

dx.doi.org/10.1021/ja3017158 | J. Am. Chem. Soc. 2012, 134, 8617−8624

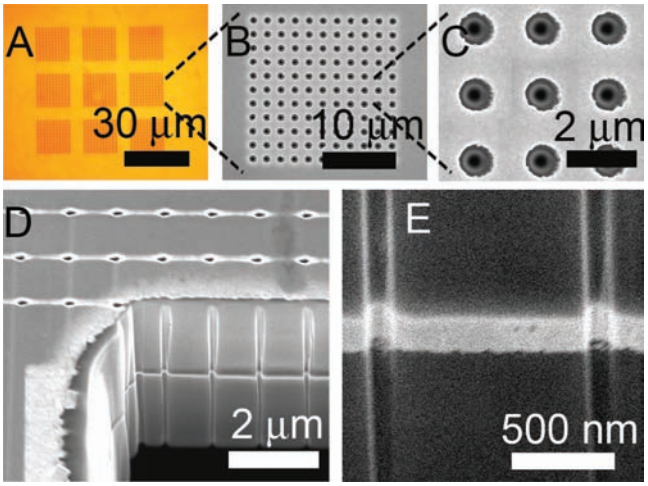

Figure 2. Fabrication characterization. (A) Reflected light micrograph of nine pore arrays; (B) SEM of a single pore array, 11 × 11 pores; (C) increased magnification; (D) SEM image of a sacrificial sample at 15° tilt, cross-sectioned by FIB milling; (E) magnified view of the EANE at 52° tilt.

Two parallel current pathways are modeled as shown in Figure 1B: the primary pathway, which results in faradaic coupling to solution, is shown by a pair of Randles circuit components and the solution resistance R_s in series. The QRE (1) and the EANE (2) are each assumed to display a double layer capacitance $C_{DL1,2}$, charge transfer resistance $R_{1,2}$, and a constant phase element $CPE_{1,2}$. A background ohmic pathway, R_b, is also present which connects the QRE and the EANE directly. The latter is caused by deposition of conductive material onto the nanochannel walls during the FIB milling step. This high-conductivity pathway was greatly diminished by flushing the completed structure in 20% aqueous HNO_3 for 5 min, which reduced the conductivity of a dry device from ~10 kΩ before cleaning to ~1 GΩ after cleaning (see SI). However, the total current i_T is the sum of the faradaic current, i_f, and the background ohmic current, i_b; therefore, a linear subtraction of the experimentally measured background current is performed,

$$i_f = i_T - i_b \quad (1)$$

RESULTS AND DISCUSSION

To characterize the response of the NCAM-EANE array, cyclic voltammetry was performed on various concentrations of $Fe(CN)_6^{4-}$ in 1.0 M KNO_3, adjusted to pH 6.65 in 10 mM phosphate buffer, Figure 3A,B. The magnitude of the background current i_b was measured using a solution of 1.0 M KNO_3 (no ferrocyanide), and is shown in Figure 3A by the black curve. Subtracting the background current from the total measured current, i_T, in Figure 3A yields the Faradaic current at the EANEs, as shown in Figure 3B (eq 1). Despite this correction, the steady state CVs in Figure 3B diverge significantly from the sigmoidal response expected for a reversible redox couple at an ultramicroelectrode. Near $E \sim 0$ V versus QRE, a large positive slope is observed before leveling off near +0.1 V, likely indicating that the equilibrium potential of the $FeCN_6^{4-}/Fe(CN)_6^{3-}$ is ~0 V versus the QRE. The proximity of the QRE to the EANE and the use of a two electrode configuration make accurate determination of the reference potential difficult. However, because the NCAM-EANE is designed for electrochemical processing, rather than analytical measurements, the focus is on other performance metrics, for example, current density, conversion efficiency, and so forth. Relevant performance metrics for the present structure are summarized in Table 1.

Near $E \sim 0.4 \pm 0.1$ V versus QRE, the slope of the $i-V$ curve again increases, as expected. As a point of reference, $i_f \sim 260$ nA, at +0.5 V versus QRE in 100 mM ferrocyanide, giving a current density, $j \sim 0.55$ A/cm^2. Importantly, the current continues to increase as the potential becomes more anodic, rather than leveling off at a diffusion-limited steady-state current to produce a sigmoidal current signature. The

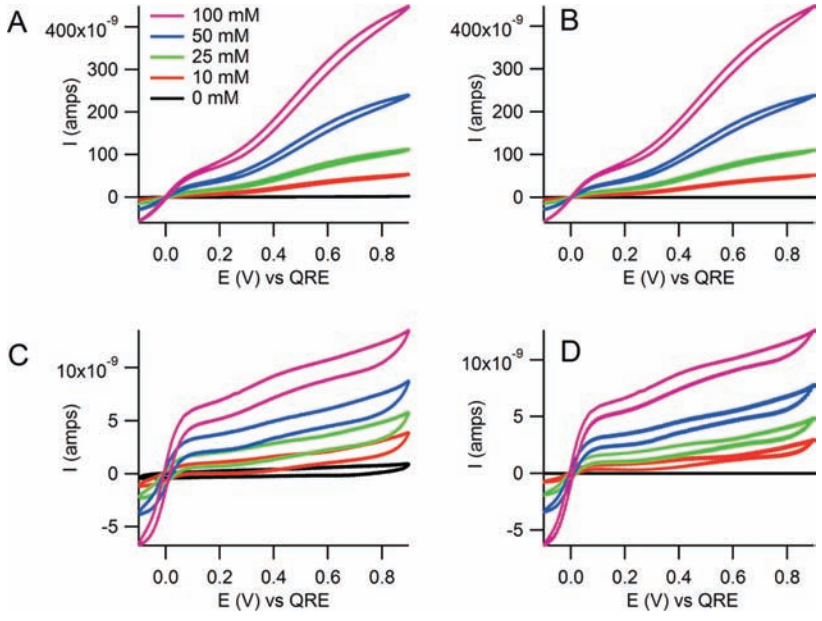

Figure 3. Cyclic voltammetry characterizing EANE performance. All solutions contain 1.0 M KNO_3 supporting electrolyte, and various concentrations of $Fe(CN)_6^{4-}$ shown in color. Scan rate is 50 mV/s. (A and B) Solutions are adjusted to pH 6.65 by addition of 10 mM phosphate buffer; (C and D) 10 mM citrate buffer, pH = 3.25 (*use caution when lowering the pH of ferricyanide solution*). (A and C) uncorrected; (B and D) after background subtraction of background CVs with no ferricyanide, i.e., the 0 mM curve in panels A and B.

dx.doi.org/10.1021/ja3017158 | J. Am. Chem. Soc. 2012, 134, 8617−8624

Table 1. Comparison of NCAM-EANE Arrays to a Typical Microband−Microchannel Structure

description[a]	flow condition	i_T at $\eta \approx 0.5$ V (nA)	J at $\eta \approx 0.5$ V (A·cm^{-2})	$1 - C/C_0$
EANE experiment:	pH 6.65	447	0.979	0.93 ± 0.21
121 pores	$u_{avg} \approx 1.5$ mm/s			
Pore dia = 603 ± 60 nm	pH 3.26	12.6	0.028	-
	$u_{avg} \approx 0$ mm/s			
EANE simulation:	EOF enabled	3.89 (1 pore)	1.03	0.95
1 pore	$u_{avg} \approx 1.5$ mm/s	470 (121 pores)		
Pore dia = 600 nm	EOF disabled	0.25 (1 pore)	0.066	-
	$u_{avg} \approx 0$ mm/s	30.1 (121 pores)		
Microchannel experiment:	flowing solution	3100	0.155	0.15
Width = 50 μm	$u_{avg} \approx 1.1$ mm/s			
Height = 50 μm	no flow	1510	0.0755	---
Electrode width = 40 μm	$u_{avg} \approx 0$ mm/s			
Microchannel theoretical prediction:	flowing solution	1540	0.0773	0.053
Width = 50 μm	$u_{avg} \approx 1.5$ mm/s			
Height = 50 μm				
Electrode width = 40 μm				

[a]Experimental and simulated values for the EANE are obtained from Figures 3 and 4, while experimental values for the microchannel are illustrated in Supporting Information, Figure S3. Theoretical values for the microchannel are derived from calculations using the results in ref 31.

important feature is that the convective transport rate in the EANE arrays increases linearly with potential as described by Smulochowski.[38] Thus, the increase in current results from the dependence of the convective transport rate on the applied potential, E, in contrast to convective voltammetry at typical microelectrodes, for which steady-state current is defined by a potential-independent convection rate and diffusion. The convective transport of reagents is added to normal diffusive transport, resulting in a continual increase in electrochemical current with increasing overpotential, until bubble nucleation occurs from solvent electrolysis. This type of CV has also been observed by Arrigan et al. in a different nanoporous structure and was attributed to an expanding interface between organic and aqueous phases.[39] The present structure has no phase boundaries; however, the general phenomenon of increased convection with increasing overpotential clearly plays a major role in both structures.

EOF can be switched off by manipulating the pH-dependent electroosmotic mobility of SU-8, which is stable at $\mu \approx 4.5 \times 10^{-4}$ cm^2 V^{-1} s^{-1} at neutral pH, but approaches $\mu \sim 0$ near pH 3.25.[40] Figure 3C shows an uncorrected CV in the absence of EOF at pH 3.25. In comparison to Figure 3A, a much reduced total current is observed, although close inspection of Figure 3C reveals the characteristic redox peaks associated with $Fe(CN)_6^{4-}/Fe(CN)_6^{3-}$. Background subtraction produces Figure 3D, which, when compared to Figure 3B, corroborates the important role of convective delivery of electroactive species to the EANE. Not only is a much higher current observed at neutral pH (447 nA at E = 0.9 V vs QRE) versus low pH (12.6 nA at E = 0.9 V vs QRE), but the slope of the $i-V$ curve is much smaller at low pH. Overall, the CV in Figure 3D is similar to those obtained from glass nanopore (GNP) electrodes.[25] Indeed, eliminating electroosmosis reduces the EANE to a structure which is highly analogous to the GNP, that is, a nanoscale electrode recessed a few micrometers from bulk solution. There is still some increase in current with increasing overpotential, which may be due to lingering electroosmotic mobility on the SU-8 surface. Nevertheless, the data in Figure 3 indicate that much higher (~ 35×) steady-state current densities are achieved under conditions of convective transport, than when EOF is disabled, and when EOF is disabled, the electron transfer behavior of the EANE closely resembles that of other nanoscale electrochemical devices.[39,41]

To explore this combined transport/electrochemical behavior in greater detail, finite element simulations were performed (details in SI). A cross section through the radially symmetric 2D simulation geometry is shown in Figure 4A. The color-coded concentration scale shows that ferrocyanide is depleted downstream from the EANE with a short diffusive gradient extending <0.5 μm toward the upstream side. The fluid is driven by convective transport toward the QRE, which is shown by the white arrows illustrating the combined Hagen−Poiseuille/EOF velocity profile. Figure 4B shows the simulated CV, which is comparable to the experimental CV in Figure 3B. Both are expressed as current density, since only one nanopore was simulated. No background subtraction is required for the simulated current, since the Faradaic current is computed from the flux of redox species perpendicular to the EANE boundary and contains no capacitive current contributions. Figure 4C,D shows results from the same simulation used in Figure 4A,B with EOF disabled.

dx.doi.org/10.1021/ja3017158 | J. Am. Chem. Soc. 2012, 134, 8617−8624

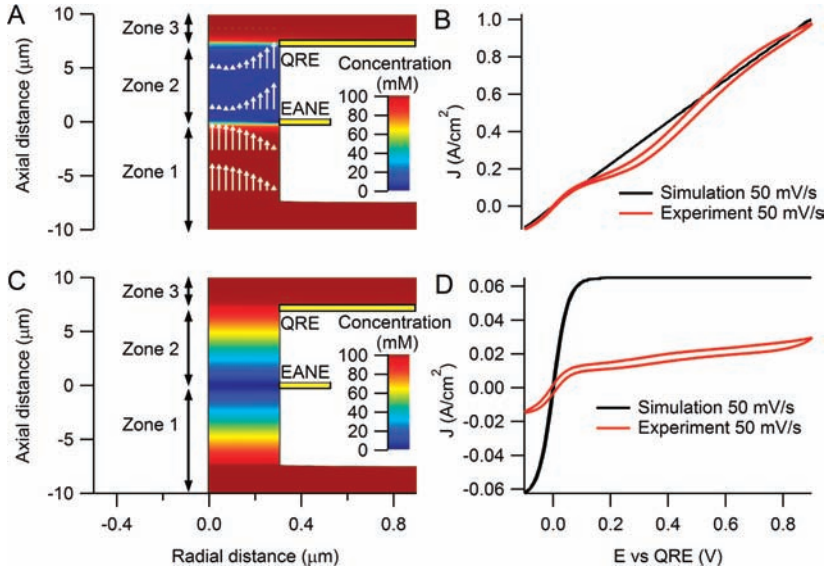

Figure 4. Simulation of electrochemistry in a single nanochannel EANE. Cyclic voltammetry is simulated at a sweep rate of 50 mV/s. (A) Cross section through the 2-D axially symmetric simulation volume, at the time coordinate corresponding to E = +0.9 vs QRE. Note the unequal scaling of the r- vs z-axes. Color scale shows concentration of the reduced species, $Fe(CN)_6^{4-}$. (A and B) Electroosmosis enabled, $\mu_{eo} = 4.5 \times 10^{-4}$ cm^2 V^{-1} s^{-1}. The white arrows indicate the velocity field; average velocity is $u_{avg} \approx 1.5$ mm s^{-1}. (B) Cyclic voltammetry corresponding to the simulation in panel A, in addition to experimental data. (C and D) Same as panels A and B but with electroosmosis disabled, $\mu_{eo} \sim 0$.

The geometry in Figure 4A,C is divided into three zones according to the relevant transport properties. In zone 1, including the bottom microchannel and the section of the nanopore preceding the EANE, there is no electric field, and convective transport is dominated by Hagen−Poiseuille flow, which is dictated by continuity at the boundary of zone 2. In zone 2, the electric field strength reaches 1.3 kV/cm, that is, E = 0.9 V dropped over ∼7 μm between the EANE and QRE, which is effective for driving EOF. Electrophoretic transport of the anionic reactant can also occur in zone 2. However, given the large pore size (∼600 nm) versus the Debye length (<5 nm) in the device, EOF is expected to dominate. Experimental results confirm this, because no current enhancement is observed at low pH in the absence of EOF, Figure 3C,D. Thus, electrophoretic motion was not included in simulations. We must also consider the possibility, in light of the short separation distance between the two electrodes, that redox cycling between the WE and QRE might occur. This possibility was accounted for in the simulations shown in Figure 4. However, since the upstream microchannel (Zone 3) is prefilled with a high concentration of reactant, back diffusion of rereduced species at the QRE is indistinguishable from the reduced species originally located in the upstream microchannel. Indeed, simulations with and without the reverse reaction occurring at the QRE are indistinguishable. Zone 3 is the upstream microchannel, which has negligible flow and merely acts as a reservoir for the solution transported through the nanopore.

In comparing Figure 4A to Figure 4C, a much larger depletion region is observed when electroosmosis is disabled, extending symmetrically several micrometers from the EANE into Zones 1 and 2. The diffusive gradient, dC/dz, is correspondingly much shallower in Figure 4C than in Figure 4A, indicating a smaller driving force for limiting electrochemical current when EOF is disabled. When EOF is enabled, the limiting current density simulated in Figure 4B shows excellent agreement with experiment (Table 1, i_f = 470 nA vs 447 nA). Similarly, the calculated and experimental limiting current density (j = 1.03 A/cm^2 vs 0.98 A/cm^2) and conversion efficiency ($(1 - C/C_0)$ = 0.95 vs 0.93) are in good agreement, and indicate exceptionally efficient throughput of the reactant to the receiving microchannel. The calculation of conversion efficiency for the experiment is straightforward (eq 2 and 3),

$$C = C_0 - \frac{i_f}{nFQ} \tag{2}$$

$$Q = \frac{1}{4}\pi R^2 N \mu_{eo} \frac{E}{h} \tag{3}$$

where n is the number of electrons transferred, F is Faraday's constant, Q is the flow rate, R is the nanopore radius, N is the number of nanopores, μ_{eo} is the electroosmotic mobility, E is the potential, and h is the distance between the EANE and the QRE. The factor of 1/4 in eq 3 is a result of the combined EOF/Hagen−Poiseuille flow profile. The calculated conversion efficiency for the simulation $(1 - C/C_0)$ uses a downstream concentration C sampled within the nanochannel, downstream from the EANE (blue region in Figure 4A). The concentration in Zone 3 was not used, because the product concentration in Zone 3 was diluted by the large volume containing reagent species. In an actual experiment operating under pseudo-steady-state conditions, the downstream product would eventually accumulate above the QRE in the absence of redox cycling, or maintain a microenvironment as shown in Figure 4A if complete reduction of the product were to occur at the QRE.

When electroosmotic flow is disabled, the limiting current density indicated in Figure 4D is j = 0.066 A cm^{-2} for the simulation (j = 0.028 A cm^{-2} for experimental data), more than an order of magnitude less than that in Figure 4B (j = 1.03 A cm^2). The ∼2× discrepancy between simulation and experiment in Figure 4D is similar to that observed previously by other groups using diffusion-limited nanoelectrode arrays.[39,41] Both groups attributed the discrepancy to overlapping diffusion

dx.doi.org/10.1021/ja3017158 | J. Am. Chem. Soc. 2012, 134, 8617−8624

zones from adjacent nanoelectrodes. Other possible explanations for the discrepancy include hindered diffusion through the long aspect ratio nanopores and/or electrostatic gating of electroactive species; however, since the goal of this work primarily targeted EOF, detailed study of the diffusion-only case was not performed.[28] Furthermore, a small difference is observed between forward and reverse scans in the experiment (50 mV/s), but not in the simulation. Several factors may contribute to the hysteresis observed experimentally: electrolysis, double layer charging, or polarization of the QRE, and the value of the electroosmotic mobility, $\mu_{eo} = 4.5 \times 10^{-4}$ cm^2 V^{-1} s^{-1} may not be accurate under these conditions.[40] Overall, both the experiment and simulations indicate a greatly enhanced steady state current density when electroosmosis is enabled, signifying the importance of convective delivery of electroactive species in nanoscale electrochemical processing.

A microband electrode−microchannel system was constructed in order to compare its performance in convective voltammetry to the NCAM-EANE array. Table 1 summarizes the Faradaic current, i_f, current density, j, and conversion efficiency, $(1 - C/C_0)$, as a function of structure (NCAM-EANE vs microchannel) and flow conditions. Overall, the NCAM-EANE shows a higher conversion efficiency than a typical microband/microchannel geometry (0.93 ± 0.21 versus 0.15). The uncertainty within the experimental EANE conversion efficiency is calculated from variability in the nanopore diameter. When the simulated EANE is compared to a hypothetical microchannel analyzed by dimensional analysis,[32] the conversion efficiency further improves for the EANE, at 0.95 versus 0.053. A higher current is observed within microband/microchannel structures than the NCAM-EANE, but the current density and conversion efficiency metrics both favor the NCAM-EANE. The improved conversion efficiency of the EANE, despite the microband electrode's much greater active area ($A_{microband} \approx 2 \times 10^{-5}$ cm^2 vs $A_{EANE} \approx 4.6 \times 10^{-7}$ cm^2), is a direct result of the much greater surface to volume ratio observed within nanofluidic structures. A separate study is ongoing which carries out a complete dimensional analysis of the EANE targeting optimization of the pore diameter, electrode height, and flow rate with respect to the dimensionless current and conversion efficiency.[42]

To independently demonstrate the usefulness of EANE arrays for electrochemical processing, the reduction of H_2O to form H_2 as a downstream processing reagent was explored.

$$2H_2O + 2e^- \leftrightarrows H_{2(aq)} + 2OH^-; \quad E^*_0 = -0.8277\ \text{V},\ E_{0,QRE} \approx 0\ \text{V} \qquad (4)$$

H_2 production from water electrolysis serves both as a model reaction system and as the basis for nanofluidic hydrogenation reactions with *in situ* reagent generation.[33] In this device, 9 blocks of 121 pores were milled (1089 pores total), each exhibiting a nanopore diameter of approximately 500 nm, resulting in a total EANE area of 3.4×10^{-6} cm^2. Figure 5 shows EANE-mediated CVs from a solution containing 15 mM phosphate buffer (pH = 5.92) and 50 μM fluorescein isothiocyanate. To prevent the reduction of dissolved O_2, which is more thermodynamically favorable than eq 4,[43] the electrolyte solution was rigorously deoxygenated prior to electrolysis, and the entire device was operated within a N_2-purged container. In Figure 5A, an extended scan range is employed to include highly reductive potentials from −1.5 V up to the slightly oxidative potential +0.5 V versus QRE. A large

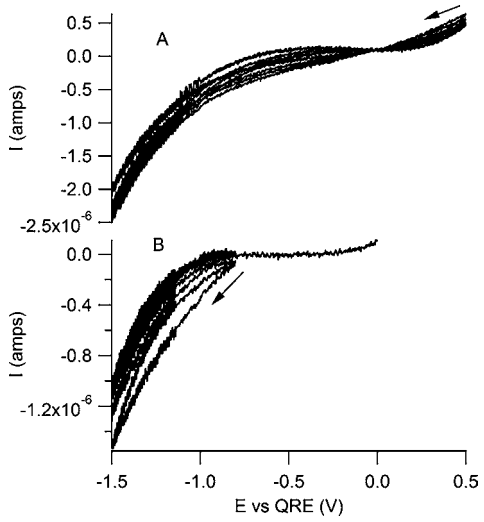

Figure 5. CV scans from a 15 mM aqueous phosphate buffer initially at pH 5.96 and 50 μM fluorescein isothiocyanate, at a scan rate of 10 mV s^{-1}. (A) Wide range of potential, scanning from +0.5 V to −1.5 V vs QRE. (B) Reductive potential scan, from −0.8 V to −1.5 V vs QRE. The final scan is extended to 0 V to illustrate the stability of the QRE in comparison to panel (A). In both plots, arrows indicate the starting scan direction.

reductive current, associated with H_2 production, is observed at potentials cathodic of −1.0 V versus QRE, while a smaller current, which is associated with electroreduction of water at the QRE, instead of the EANE, is observed at anodic potentials. Since it is desired that H_2 production occur only at the embedded electrode, a second experiment was performed over a more cathodic range, from −1.5 V to −0.8 V versus QRE, Figure 5B, in order to avoid H_2O reduction at the QRE. These results show a similar level of reduction current as in Figure 5A. In both panels A and B of Figure 5, subsequent scans show a decreasing faradaic current, that likely results from polarization of the QRE, with possible contributions from titration of electroosmotic mobility near the QRE or degradation of the electrodes.

The solution composition was probed with the pH-dependent emission of fluorescein.[44,45] Since OH^- is produced in a 2:1 stoichiometric ratio with dissolved H_2 and the quantum efficiency of fluorescein is pH-dependent,[45] emission measurements can be used to indicate the rate of H_2 production. Figure 6A,B shows the applied potential program and resulting integrated fluorescence versus time, respectively, during the CV scan in Figure 5A. Two frames from the fluorescence emission movie, representing the cathodic (Figure 6C, E_{appl} = −1.5 V vs QRE) and anodic (Figure 6D, E_{appl} = +0.5 V vs QRE) ends of the CV scan, respectively, are also displayed. At cathodic potentials, Figure 6B t = 200 s, a moderately enhanced fluorescence intensity is apparent, consistent with reduction of H_2O and concomitant production of OH^- at the EANE. However, a larger enhancement is observed at the anodic end of the scan (t = 400 s). This anodic enhancement was unexpected, because a larger current is observed at cathodic potentials in Figure 5A. The discrepancy is caused by the fluorescence collection efficiency, which is much lower for fluorophores at the EANE in the center of the nanochannel, than at the QRE. Any enhanced emission from the high-pH region within the nanopores must escape an aperture slightly smaller than the emission wavelength (d = 500 nm vs $\lambda \approx$ 550

dx.doi.org/10.1021/ja3017158 | J. Am. Chem. Soc. 2012, 134, 8617−8624

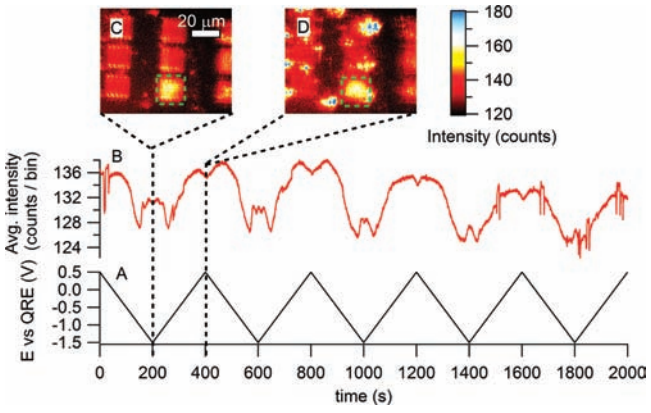

Figure 6. Fluorescence images and temporal intensities corresponding to the CV in Figure 5A. (A) E_{appl} vs time; (B) average fluorescence intensity vs time; (C) fluorescence image at t = 200 s (E_{appl} = −1.5 V vs QRE); (D) fluorescence image at t = 400 s (E_{appl} = +0.5 V vs QRE). Excitation radiation is focused on, and fluorescence intensity trace is acquired over, the area highlighted in the dotted green boxes in panels C and D. Emission intensity is displayed on a color scale.

nm) at a level which is higher than the foreground of fluorescein-containing solution between the QRE and the microscope objective, Figure 1A. Care was taken to minimize this foreground fluorescence by illuminating the sample diascopically. In addition, when the EANE is held at negative potentials relative to the QRE, EOF transports the high fluorescence liquid away from the QRE and the observation side of the device (see Figure 1). Despite these limitations, enhanced emission is still observed during reduction steps. In comparison, the fluorescence enhancement observed at high potential represents an increase in pH at the QRE from which fluorescence collection is unhindered. Therefore, both regions show an enhanced concentration of hydrogen, but a quantitative comparison cannot be made because the microscope renders fluorescence intensity from the two regions differently.

Figure 6 also illustrates an advantage of EOF in nanopores when used for H_2 production. When the EANE is held at an anodic potential relative to the QRE, bubbles may nucleate at the QRE, caused by H_2O reduction at the QRE (not the EANE). These bubbles are also responsible for the instabilities in the fluorescence signal at oxidative potentials, for example, at t = 1500 s in Figure 6D. Conversely, no H_2 bubbles are observed during electrolytic H_2 production at the EANE as shown in Figures 3 and 4. The high EOF rate through the pores acts in concert with other factors, such as surface tension and diffusion of H_2 into the surrounding polymer, to prevent bubble formation. Further, because the concentration necessary to effect a significant change in the buffer pH is of the same order as the buffer concentration, 15 mM, the enhanced fluorescence region at t = 200 s can be assigned to an H_2-rich microenvironment with a [H_2] of at least several mM. This enrichment is comparable to that obtainable from high pressure H_2 gas and is sufficient for hydrogenation reactions.[13]

Since many of the artifacts related to bubble formation at the QRE are undesirable, a second set of electrolytic scans was run, scanning the more cathodic region −0.8 V to −1.5 V versus QRE (Figure 5B, fluorescence data in SI). Under these conditions, no bubble formation is observed at the QRE, while the fluorescence shows a similar enhancement to that in Figure 6B at reductive potentials. Under these conditions, a significant concentration of H_2 is again generated within the nanofluidic volume, sufficient for downstream processing of hydrogenation reactions within nanofluidic channels.[46]

CONCLUSIONS

The construction and characterization of NCAM-EANE arrays demonstrate that electron transfer reactions and electrokinetic flow control can be coupled productively to achieve greater than an order of magnitude increase in current density, compared to nanoelectrodes within diffusion-limited nanofluidic volumes. The high pore density, parallel arrays of electrochemically active nanopores can be inserted between microfluidic layers, to produce new functionality, namely, electrochemical reactive processing in three-dimensional μTAS structures. Fluorescence results indicate that electrolysis of H_2O results in *in situ* H_2 generation at concentrations ranging up to millimolar levels without bubble formation, concentrations sufficient for enhanced downstream processing in the nanoconfinement of the NCAM. Thus, the enhanced electrochemical signal resulting from concurrent EOF and electrochemistry at a nanoelectrode inside a nanochannel extends the utility of hybrid nano-microfluidic structures to situations where electrochemical processing is needed.

ASSOCIATED CONTENT

Supporting Information

Details regarding chemicals and reagents, microfluidic channel assembly, electrochemical parameters, construction of the fluorescence microscope, methods used in numerical simulation, and additional fluorescence data. This material is available free of charge via the Internet at http://pubs.acs.org.

AUTHOR INFORMATION

Corresponding Author

pbohn@nd.edu

Notes

The authors declare no competing financial interest.

ACKNOWLEDGMENTS

We gratefully acknowledge financial support from the U.S. Department of Energy Basic Energy Sciences (DE FG02 07ER15851) and from the U.S. National Science Foundation Water CAMPWS (CTS0120978).

REFERENCES

(1) Arrigan, D. W. M. *Analyst* **2004**, *129*, 1157.
(2) Murray, R. W. *Chem. Rev.* **2008**, *108*, 2688.
(3) Lohmuller, T.; Muller, U.; Breisch, S.; Nisch, W.; Rudorf, R.; Schuhmann, W.; Neugebauer, S.; Kaczor, M.; Linke, S.; Lechner, S.; Spatz, J.; Stelzle, M. *J. Micromech. Microeng.* **2008**, *18*, No. 115011.
(4) Baranski, A. S.; Krogulec, T.; Nelson, L. J.; Norouzi, P. *Anal. Chem.* **1998**, *70*, 2895.
(5) Lemay, S. G.; Goluch, E. D.; Wolfrum, B.; Singh, P. S.; Zevenbergen, M. A. G. *Anal. Bioanal. Chem.* **2009**, *394*, 447.
(6) Wang, X. Y.; Cheng, C.; Wang, S. L.; Liu, S. R. *Microfluid. Nanofluid.* **2009**, *6*, 145.
(7) Lastochkin, D.; Zhou, R. H.; Wang, P.; Ben, Y. X.; Chang, H. C. *J. Appl. Phys.* **2004**, *96*, 1730.
(8) Lee, T. T.; Dadoo, R.; Zare, R. N. *Anal. Chem.* **1994**, *66*, 2694.
(9) Piruska, A.; Branagan, S.; Cropek, D. M.; Sweedler, J. V.; Bohn, P. W. *Lab Chip* **2008**, *8*, 1625.
(10) Dhopeshwarkar, R.; Hlushkou, D.; Nguyen, M.; Tallarek, U.; Crooks, R. M. *J. Am. Chem. Soc.* **2008**, *130*, 10480.

(11) Sheridan, E.; Hlushkou, D.; Anand, R. K.; Laws, D. R.; Tallarek, U.; Crooks, R. M. *Anal. Chem.* **2011**, *83*, 6746.
(12) Han, J.; Schoch, R. B.; Cheow, L. F. *Nano Lett.* **2007**, *7*, 3895.
(13) Kappe, C. O.; Desai, B. *J. Comb. Chem.* **2005**, *7*, 641.
(14) Henry, C. S.; Holcomb, R. E.; Kraly, J. R. *Analyst* **2009**, *134*, 486.
(15) Livak-Dahl, E.; Sinn, I.; Burns, M. *Annu. Rev. Chem. Biomol. Eng.* **2011**, *2*, 325.
(16) Gatimu, E. N.; Jin, X. Z.; Aluru, N.; Bohn, P. W. *J. Phys. Chem. C* **2008**, *112*, 19242.
(17) Sweedler, J. V.; Kuo, T. C.; Cannon, D. M.; Chen, Y. N.; Tulock, J. J.; Shannon, M. A.; Bohn, P. W. *Anal. Chem.* **2003**, *75*, 1861.
(18) Fa, K.; Tulock, J. J.; Sweedler, J. V.; Bohn, P. W. *J. Am. Chem. Soc.* **2005**, *127*, 13928.
(19) Kim, S. J.; Wang, Y. C.; Lee, J. H.; Jang, H.; Han, J. *Phys. Rev. Lett.* **2007**, *99*, 044501.
(20) Jacobson, S. C.; Kovarik, M. L. *Anal. Chem.* **2008**, *80*, 657.
(21) Sinton, D.; Gordon, R.; Brolo, A. G. *Microfluid. Nanofluid.* **2008**, *4*, 107.
(22) Erickson, D.; Choi, I.; Huh, Y. S. *Lab Chip* **2011**, *11*, 632.
(23) Wang, Z.; King, T. L.; Branagan, S. P.; Bohn, P. W. *Analyst* **2009**, *134*, 851.
(24) Yeh, J. I.; Shi, H. B. *Wires Nanomed. Nanobioltechnol.* **2010**, *2*, 176.
(25) Zhang, B.; Zhang, Y. H.; White, H. S. *Anal. Chem.* **2004**, *76*, 6229.
(26) White, H. S.; Zhang, B.; Zhang, Y. H. *Anal. Chem.* **2006**, *78*, 477.
(27) White, H. S.; Bund, A. *Langmuir* **2008**, *24*, 12062.
(28) White, H. S.; Bund, A. *Langmuir* **2008**, *24*, 2212.
(29) Lanyon, Y. H.; De Marzi, G.; Watson, Y. E.; Quinn, A. J.; Gleeson, J. P.; Redmond, G.; Arrigan, D. W. M. *Anal. Chem.* **2007**, *79*, 3048.
(30) Holtzel, A.; Tallarek, U. *J. Sep. Sci.* **2007**, *30*, 1398.
(31) Gatimu, E. N.; Sweedler, J. V.; Bohn, P. W. *Analyst* **2006**, *131*, 705.
(32) Amatore, C.; Da Mota, N.; Sella, C.; Thouin, L. *Anal. Chem.* **2007**, *79*, 8502.
(33) Contento, N. M.; Branagan, S. P.; Bohn, P. W. *Lab Chip* **2011**, *11*, 3634.
(34) Jonsson, M. P.; Dahlin, A. B.; Feuz, L.; Petronis, S.; Hook, F. *Anal. Chem.* **2010**, *82*, 2087.
(35) Piruska, A.; Branagan, S. P.; Minnis, A. B.; Wang, Z.; Cropek, D. M.; Sweedler, J. V.; Bohn, P. W. *Lab Chip* **2010**, *10*, 1237.
(36) Abgrall, P.; Lattes, C.; Conederal, V.; Dollat, X.; Colin, S.; Gue, A. M. *J. Micromech. Microeng.* **2006**, *16*, 113.
(37) Shinwari, M. W.; Zhitomirsky, D.; Deen, I. A.; Selvaganapathy, P. R.; Deen, M. J.; Landheer, D. *Sensors* **2010**, *10*, 1679.
(38) Squires, T. M.; Bazant, M. Z. *J. Fluid Mech.* **2004**, *509*, 217.
(39) Rimboud, M.; Hart, R. D.; Becker, T.; Arrigan, D. W. M. *Analyst* **2011**, *136*, 4674.
(40) Sikanen, T.; Tuomikoski, S.; Ketola, R. A.; Kostiainen, R.; Franssila, S.; Kotiaho, T. *Lab Chip* **2005**, *5*, 888.
(41) Godino, N.; Borrise, X.; Munoz, F. X.; del Campo, F. J.; Compton, R. G. *J. Phys. Chem. C* **2009**, *113*, 11119.
(42) Gibson, L.; Branagan, S.; Bohn, P. W. *Small*, submitted for publication.
(43) Mitrovski, S. M.; Nuzzo, R. G. *Lab Chip* **2005**, *5*, 1184.
(44) Raines, R. T.; Lavis, L. D.; Rutkoski, T. J. *Anal. Chem.* **2007**, *79*, 6775.
(45) Lee, D. H.; Sung, H. J.; Han, D. W.; Lee, M. S.; Ryu, G. H.; Aihara, M.; Takatori, K.; Park, J. C. *Yonsei Med. J.* **2005**, *46*, 268.
(46) Huang, C. P.; Wang, D. M.; Shah, S. I.; Chen, J. G. *Sep. Purif. Technol.* **2008**, *60*, 14.